Ab initio calculations of the optical and electronic properties of Bi_2WO_6 doped with Mo, Cr, Fe, and Zn on the W–lattice site

V. Koteski, J. Belošević-Čavor, V. Ivanovski, A. Umićević, D. Toprek
Vinča Institute of Nuclear Sciences, University of Belgrade, 11001 Belgrade, Serbia

---

Abstract

Substitutionally doped $Bi_2W_{1-x}M_xO_6$ (M = Mo, Cr, Fe, Zn; $x = 0.125$, 0,25, 0.5) is investigated using the density functional theory (DFT). For all the investigated transition metal dopants, the optical properties in the visible light range are improved over the undoped Bi_2WO_6. Irrespective of concentration, the lattice relaxation around the dopants is constrained to the first coordination shell. Mo, Fe, and Cr introduce localized defect states in the band gap, contributing to band gap narrowing. The localized states are hybridized between the impurity *d*–bands and host W 5*d*– and O 2*p*–states. Zn facilitates the reduction of the band gap by inducing a shift of the states near the top of the valence band toward higher energies. Our results suggest that Zn doping on the W lattice site may improve the photocatalytic properties of Bi_2WO_6 more than the other dopants.

---

1. Introduction

Recently, there has been a growing interest in developing efficient visible light driven photocatalysts that would be used for decomposition of organic pollutants and photocatalytic hydrogen production [1]. While TiO_2 is a superior photocatalyst for fuel cell production, water treatment, environmental protection, and other applications, it is mainly active under ultraviolet radiation which is less than 5 percent of the total solar radiation. Therefore, one of the main goals of visible light photocatalysis is searching for TiO_2 alternatives that can use solar energy more effectively. Among the promising materials for visible light spectrum photocatalysis is Bismuth tungstate (chemical formula Bi_2WO_6), which exhibits excellent performance in the photodegradation of pollutants under visible light [2–5] and a notable activity to inactivate Escherichia coli [6].

Bi_2WO_6 belongs to the class of perovskite-like Aurivillius compounds of $Bi_2A_{n-1}B_nO_{3n+3}$ type (A and B are cations with different atomic coordination). In the case of Bi_2WO_6, W is a 6–fold coordinated atom positioned in the center of an oxygen octahedron and $n = 1$. The structure is presented in Fig. 1 and constitutes of WO_4^{2-} perovskite-like layers alternating $Bi_2O_2^{2+}$ fluorite-like layers.

Apart from single crystals, Bi_2WO_6 comes in many different forms, including nano-particles, nano-plates, helix-like structures, flower-like structures, thin films, and other superstructures [7]. Even though Bi_2WO_6 can absorb in the visible range, its photocatalytic activity is still low to be comparable to that of TiO_2 [8]. This is mostly due to its high electron/hole recombination rate, which is a result of the relatively low potential of the Bi_2WO_6 conduction band which prevents the trapping of activated electrons by O_2 to form superoxide ion ${O_2}^{2-}$ [2, 8]. The photocatalytic performance strongly depends on the structure, shape, and form of the material, but it can also be affected by incorporating foreign atoms.

Foreign dopants, more than the structure itself, can help improve the electron-hole lifetimes and expand the region responsive to visible light, thereby improving the overall photocatalytic activity. With regard to the improvement of the photocatalytic properties, the dopants may also play a crucial role by changing the position of its levels in the valence band (VB), within the band gap, or in the conduction band (CB). The dopant levels may also expand or shorten the width of the valence or conduction band, directly affecting the mobility of the photogenerated charges.

Doping has been a widely used strategy to decrease the recombination of photoinduced electron-hole pairs in Bi_2WO_6. For instance, Tian et al. showed that

Gd doping has great influence on the photocatalytic activity and microstructure of Bi_2WO_6 [9]. Guo et al. successfully produced Fe–ions modified Bi_2WO_6 nanosheets, with improved photocatalytic activity for the degradation of gaseous toluene [10]. Zhang et al. demonstrated that $Bi_2Mo_{0.25}W_{0.75}O_6$ shows much higher activity than Bi_2WO_6 under visible light [11]. Shi et al. showed that the photocatalytic activity of F^- substituted Bi_2WO_6 for degradation of methylene blue under visible light irradiation increased about two times compared to pure Bi_2WO_6 [12]. Doping Bi_2WO_6 with Br also proved to be a way to produce samples with better photocatalytic activity [13, 14]. Also it has been reported that doping Bi_2WO_6 with many other metals, such as Lu [15], Ag [16], Cu [17], Mo [18], Zn [19], Zr [20], Er [21–23], Pt [24], Sr [25], Cd [26], Eu, La [27], and Ba [28] raised the degradation rate of pollutants under visible light. Several studies of codoped Bi_2WO_6 [21, 29, 30] also exist in the literature.

In this work we investigate the changes in structural, electronic, and optical properties of Bi_2WO_6 upon doping with Cr, Mo, Fe, and Zn transition metals. The electronic properties of the system are strongly affected by the new chemical environment established by the dopants. After replacing one or several W atoms with transition metals, we calculated the changes in the corresponding bond lengths, band structure, density of states (DOS), and optical absorption coefficients. Cr and Mo were chosen as isoelectronic elements with respect to the host constituent, W. Fe is often used in doping of various material. Zn, with its electronic configuration of occupied dopant states ($3d^{10}$) in the valence band, is a good candidate for reducing the band gap, as observed in a previous study [30, 31] for substitution on the Bi lattice site.

2. Calculation details

The calculations presented in this paper were performed using the Vienna *ab initio* simulation package VASP [32, 33]. VASP employs Projector Augmented Wave (PAW) pseudopotentials and plane waves to calculate the ground state properties of crystalline structures. The exchange and correlation effects

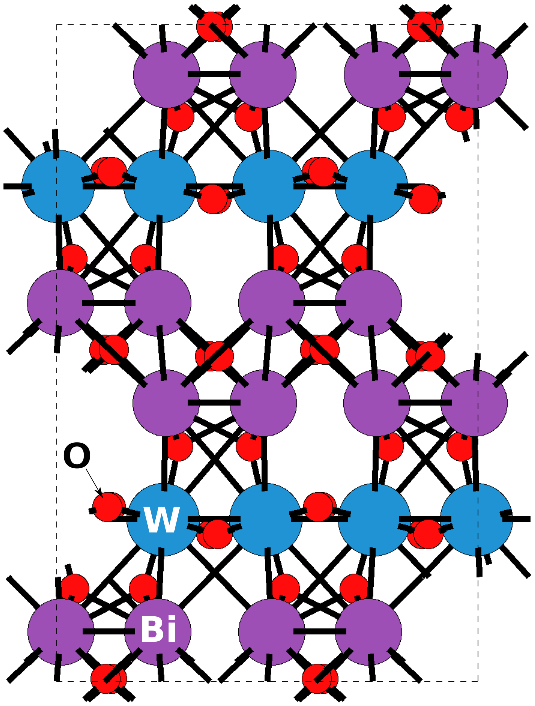

Figure 1: Crystal structure of Bi_2WO_6 projected onto the *ac* plane.

of the electronic system were accounted for within the generalized gradient approximation (GGA) in its PBE [34] implementation. In the calculation of the *DOS* we also used hybrid functionals to be able to give more accurate prediction of the size of the band gap and the position of the individual dopant levels. A cut-off energy of 300 eV along with a MonkhorstPack [35] k–point mesh of 7×3×7 k–points for the pure system and 3×2×7 k–points for the doped systems calculations were chosen.

3. Structural Properties

Bi_2WO_6 crystallizes into the space group $P21ab$ (No. 29) [36, 37]. It is characterized by an orthorhombic unit cell with 36 atoms. The calculated lattice parameters (a = 5.437, b = 5.622, and c = 16.923 Å) are in good agreement with the experimental ones [36, 37] and the previously reported calculated ones [38]. The impurity system was modeled by incorporating the dopant atoms in a 72–atom supercell with 2×1×1 geometry. As an example, the different arrangements of iron substituting on the tungsten sublattice are shown in Fig. 2. The a, b, and c parameters of the supercells were fixed to the values derived from the lattice parameters of the pure optimized orthorhombic unit cell. We considered three different concentrations of 12.5%, 25%, and 50% (corresponding to a replacement of 1, 2, and 4 W atoms, respectively). After the substitution, all the atoms in the supercell were allowed to relax with force minimization criterion of 0.03 eVÅ^{-1}. The atomic positions were rearranged at each ionic step according to the interatomic Hellmann-Feynman forces calculated with VASP. Using the Broyden Fletcher Goldfarb Shanno (BFGS) quasi-Newton optimization method, as implemented in the Atomic Simulation Environment python interface [39], the inner degrees of freedom of the atoms were minimized to the corresponding nearest local minima.

On average, the substituting atoms perturb the host lattice to a different extent depending on their type. Our calculations indicate that there are no sizable displacements or rearrangements of atoms. The effects of the transition

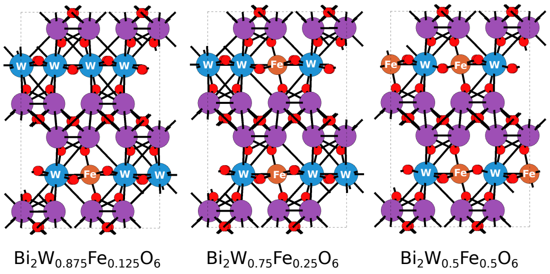

Figure 2: Different configurations of iron doped Bi_2WO_6 calculated in this work: left 12.5%, center 25%, and right 50% of W atoms replaced by Fe.

metal substitution are largely confined to the nearest neighbor (NN) atomic coordination.

Mo, as an isoelectronic dopant, seems to perturb the host lattice the least. This is reflected in the positions of the NN oxygen atoms only slightly displaced from their original lattice sites (see Tab. 1). The other isoelectronic dopant, Cr, has a considerably smaller atomic radius than W. As a result, the perturbation it induces in the lattice is larger. This is visible in the shortening of the four Cr—O bond lengths present within in the WO_4 layer. In contrast, the remaining two Cr—O bond lengths that connect chromium to the adjacent Bi_2O_2 layers are elongated. Compared to the Cr–doped systems, the structural optimization of Zn–doped Bi_2WO_6 shows that the NN oxygen atoms relax in the opposite direction: the two Zn—O bonds that bridge the WO_4 layers are shortened, while the majority of the other four distances are elongated. Fe is similar to Mo because it introduces only a very small perturbation of the NN distances. The bond lengths in Tab. 1 are given for the systems with 50% concentration of dopant atoms. It is noteworthy that nearly the same optimized distances are obtained after the lattice optimization of the supercells with 12.5% and 25% concentration of dopant atoms, indicating that the structural perturbation is localized in the vicinity of the foreign atom.

Table 1: Displacement of the 6 NN oxygen atoms after dopant substitution on the W sublattice in $Bi_2W_{0.5}M_{0.5}O_6$ (M = Mo, Cr, Fe, and Zn). The NN distances are given as percentage changes from the ideal pure host distances.

	d(Å)		d(Å)	Δd(%)		d(Å)	Δd(%)		d(Å)	Δd(%)		d(Å)	Δd(%)
W—O_1	1.877	Mo—O_1	1.893	+0.9	Cr—O_1	1.783	-5.0	Zn—O_1	1.910	+1.8	Fe—O_1	1.888	+0.6
W—O_2	1.943	Mo—O_2	1.932	-0.6	Cr—O_2	1.789	-7.9	Zn—O_2	1.935	-0.4	Fe—O_2	1.944	+0.05
W—O_3	1.789	Mo—O_3	1.757	-1.8	Cr—O_3	1.661	-7.2	Zn—O_3	1.920	+7.3	Fe—O_3	1.717	-4.0
W—O_4	1.813	Mo—O_4	1.818	+0.3	Cr—O_4	1.678	-7.4	Zn—O_4	2.055	+13.3	Fe—O_4	1.785	-1.5
W—O_5	2.120	Mo—O_5	2.153	+1.6	Cr—O_5	2.196	+3.6	Zn—O_5	1.977	-6.7	Fe—O_5	2.193	+3.4
W—O_6	2.241	Mo—O_6	2.240	-0.05	Cr—O_6	2.313	+3.2	Zn—O_6	2.084	-7.0	Fe—O_6	2.275	+1.5

4. Density of states

The standard LDA and GGA functionals, including the PBE functional used in this work, perform relatively well for structural relaxation, but when it comes to calculating the DOS of solids, they underestimate the size of the band gap [40]. In our case, the PBE calculations gave 1.4 eV for pure Bi_2WO_6, which is considerably smaller than experimental band gap that is between 2.7 and 2.9 eV, depending on the crystal state and morphology [11, 41–44]. Therefore, for the DOS calculations of the pure and doped systems, we have chosen the Heyd-Scuseria-Ernzerhof HSE06 screened hybrid functional [45]. This version is similar to the more popular PBE0 hybrid functional in terms of accuracy and thermochemistry, but it has better convergence properties [46]. First order Methfessel-Paxton smearing with smearing width of $\sigma = 0.05$ eV was used for the partial occupation of the atomic orbitals in all the DOS calculations.

Using the HSE06 functional, the size of the calculated band gap of pure Bi_2WO_6 was improved to 2.47 eV. From the DOS given in Fig. 3, it is evident that the valence band is mainly composed of O–2p–states along with a certain amount of Bi–6p– and 6s–states and W–5d–states. The conduction band is a mixture of W–5d–, O–2p–, and Bi–6p–states, which is consistent with the previously reported calculated results [3, 29].

The partial density of states ($PDOS$) presented in Fig. 4 offers additional details about the electronic structure. The doping with all the four transition metals introduces significant changes in the band gap size and shape. These

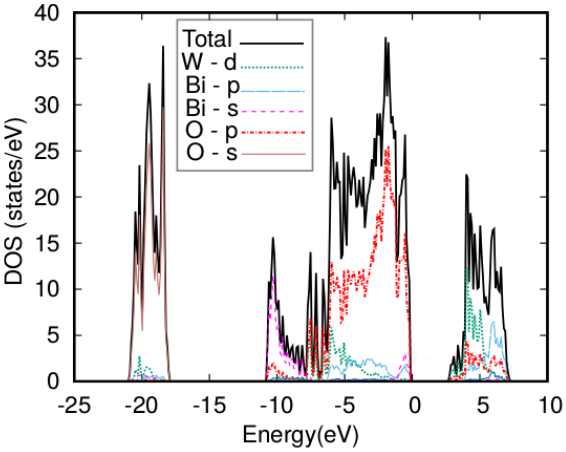

Figure 3: Density of states of undoped Bi_2WO_6 obtained with the HSE06 hybrid functional.

changes are particularly visible near the top of the VB and bottom of the CB.

Band gap reduction is observed in all the four plots, mostly due to the presence of deep impurity states in the band gap. However, the changes near the top of the VB in the Zn–doped system are not a result of a significant presence of Zn–bands. In this case, there is a split off of states near the top of the VB. This is a result of a dopant-host interaction, i.e., interaction between the Zn–3d–states situated about 7 eV below the top of the VB, and host O–2p–states close to the VB maximum.

Our calculated band gap reduction for $Bi_2W_{0.5}Mo_{0.5}O_6$ is about 10 % (band gap of 2.24 eV vs. 2.47 eV for pure Bi_2WO_6), in excellent agreement with the measurements [11, 18]. From the $PDOS$, it can be seen that Mo and Cr, with their respective 4d– and 3d–states, introduce deep levels within the band gap of Bismuth tungstate. In both cases, these levels are hybridized with the nearby O–2p– and W–5d–states. The Mo dopant levels are adjacent to the bottom of the CB and hybridize more strongly with bands of W 5d character. By comparison, the Cr–levels are further below and hybridize with the neighboring tungsten d electrons to a much smaller degree.

Iron contributes with two separate deep levels within the band gap, both of

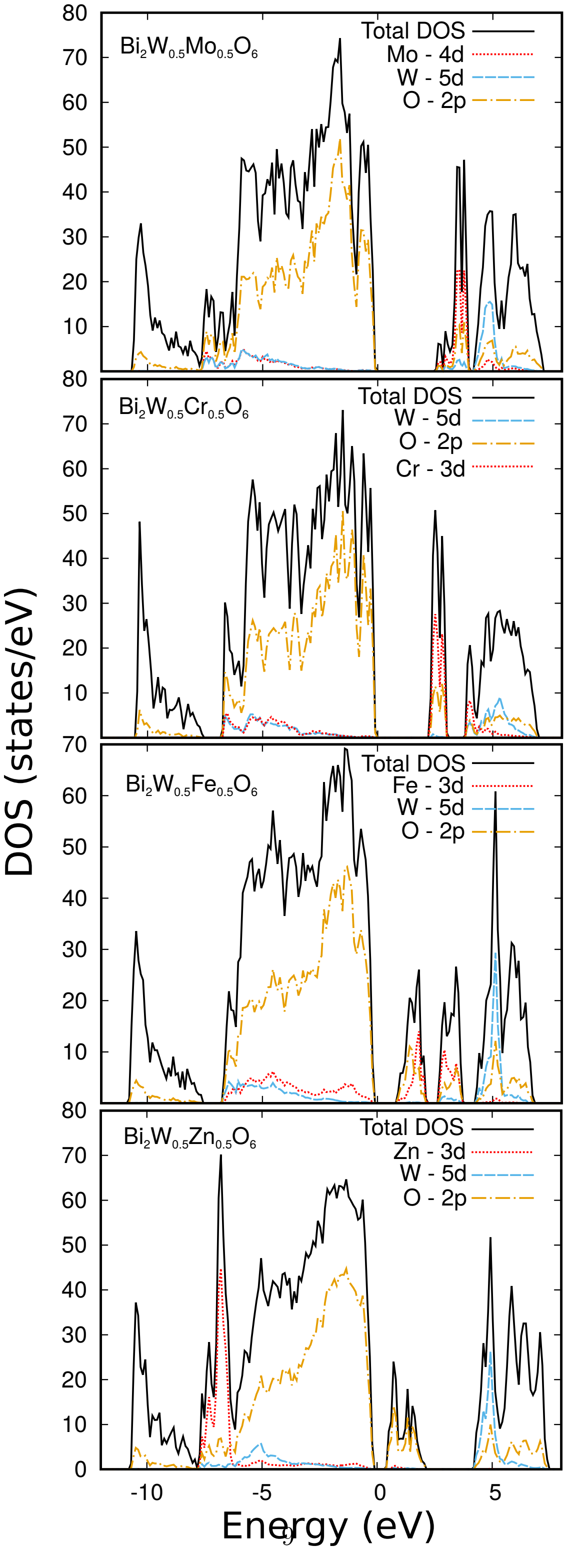

Figure 4: *PDOS* of Bi_2WO_6 using the HSE06 hybrid functional.

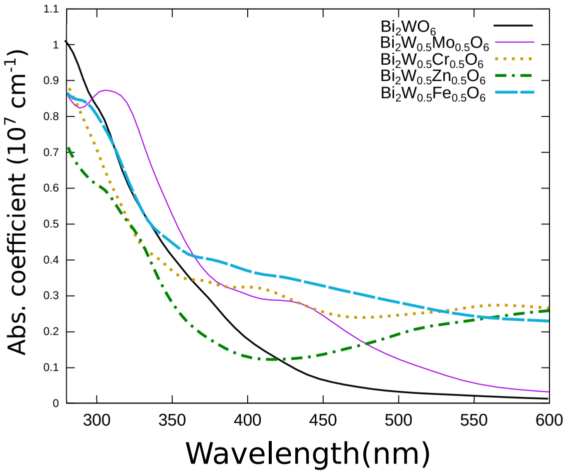

Figure 5: Optical absorption coefficient for pure Bi_2WO_6 compared to Bi_2WO_6 doped with Mo, Zn, Cr, and Fe.

which are hybridized with host bands similar to the the Cr– and Mo–doped systems. In this case, however, the impurity levels are at almost equidistant positions from the top of the VB and the bottom of the CB.

As indicated, Zn does not introduce any deep defect levels in the band gap directly. Similar electronic structure was observed in previous calculations [31] where Zn substitution on Bi lattice site was studied. This behavior could make Zn a dopant of choice, as the impurity levels in the band gap often serve as recombination centers, reducing the photocatalytic activity. ~~The excellent properties of Zn–doped Bi_2WO_6 have already been observed in some measurements, showing that the addition of 12% of Zn leads to a photocurrent enhancement of up to 80%.~~ Our HSE06 calculations indicate substantial changes at the top of the VB, a VB shift in upward direction, and a consequent band gap reduction.

However, besides the absorptivity and the mobility of photoexcited charge carriers, the photocatalytic activity of the semiconductor is also governed by the positions of its conduction band minimum (CBM) and valence band maximum (VBM). For example, the photocatalytic decomposition of organic contaminants requires that the VB of the photocatalyst must match the potential level of oxidizing the organic contaminants. The VB and CB energy level of a semiconductor can be roughly calculated from the formulas[31] $E_{VB} = E_{CB} + E_g$ and $E_{CB} = X - E_c - E_g/2$, where E_{VB} and E_{CB} are the VB and CB edge potentials, E_c is the energy of free electrons on hydrogen scale ($\sim$ 4.5 eV), E_g is the band gap energy of the semiconductor and X is its Mulliken's electronegativity (6.22 eV for Bi_2WO_6). In order to match the experimental band gap value of Bi_2WO_6, we employed 0.33 eV scissor operator. Our calculated E_{VB} for pure Bi_2WO_6 is 3.11 eV, which is more positive than the standard redox potentials of OH/OH^- (1.99 eV) and oxygen evolution (1.23 eV), meaning that Bi_2WO_6 can be used for these reactions. In contrast, its E_{CB} of 0.31 eV is not suitable for hydrogen evolution, as it is more positive than the hydrogen reduction potential. The calculated E_{VB} and E_{CB} values for Mo-doped Bi_2WO_6 are 2.95 eV and 0.38 eV, which means that its oxidation ability decreases and its reduction ability remains almost unchanged. The oxidation ability of Zn-doped Bi_2WO_6 (E_{VB} = 2.85 eV) is comparable to that of the Mo-doped system, but its reduction ability (E_{CB} = 0.56 eV) is even worse. Thus we can conclude that the enhanced photocatalytic oxidation properties of Zn-doped Bi_2WO_6 that have been observed in some measurements, [19] can be attributed exclusively to the increased visible light absorption of the Zn-doped material.

The width of the VB and CB is also affected by the dopants. A sizable reduction of the width of the VB is observed in the case of Cr and Fe doping. The width of the CB is affected to a lesser degree, but here we also observe a small reduction. In the case of Mo dopant, a very slight reduction (by 0.1 eV) of the CB width is observed, while the width of the VB remains the same. The width reduction of the VB and CB may have a huge impact on the mobility of the photogenerated charges, as the smaller widths of the VB and CB may enhance the effective mass of the photogenerated charges and diminish their mobility. In this respect, Cr and Fe may not be as ideal doping candidates as the other two dopants.

5. Optical Properties

The absorption coefficient plots of pure and doped Bi_2WO_6 as a function of incident photon wavelength are shown in Fig. 5. They were obtained within the PBE formalism from the real and imaginary parts of the dielectric function, averaged over the three polarization vectors.

As can be seen, transition metal doping on the W lattice site considerably improves the light absorption in the visible range between 400 and 700 nm. The undoped Bi_2WO_6 is found to have the lowest absorbance in this region. The steep shape of the spectra in the case of Bi_2WO_6 and $Bi_2W_{0.5}Mo_{0.5}O_6$, indicates that the absorption in these systems is not due to transitions from impurity levels, but is a result of direct band-gap transitions. The red shift of the main absorption peak and better absorption in the region between 400 and 600 nm, as compared to Bi_2WO_6, is found for $Bi_2W_{0.5}Mo_{0.5}O_6$. The obtained absorption spectrum for this system (see Fig. 5) is in excellent agreement with the corresponding spectrum obtained from the UV–vis spectroscopic measurements [47]. The absorbance of Zn–doped Bi_2WO_6 tends to increase as the wave-length increases, in contrast to the absorbance of Bi_2WO_6 doped with the other dopants, which decreases as we approach the red end of the spectrum. The different behavior of the absorption coefficient of Zn–doped Bi_2WO_6 is in agreement with the different mechanism of its band gap reduction, as suggested by the calculated electronic structure.

The absorbance does not seem to saturate much with increased dopant concentration. As an illustration, Fig. 6 depicts the absorption coefficient plots of Cr– and Zn–doped Bi_2WO_6 as a function of concentration. In general, the absorbance is improved with concentration for all the transition metals considered in this work for the majority of the visible wavelengths (Fig. 5). For the Zn-doped system, the absorbance is markedly improved with concentration in the region up to 2.9 eV (see Fig. 6, bottom), while the reverse seems to be true for energies above the visible electromagnetic spectrum.

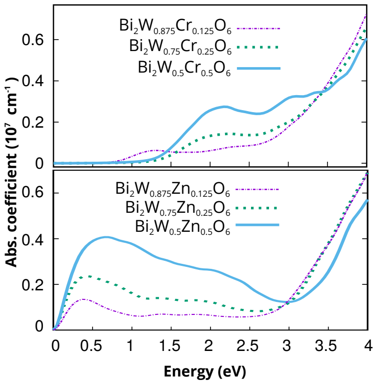

Figure 6: Optical absorption coefficient of Cr– and Zn–doped Bi_2WO_6 as a function of dopant concentration.

6. Conclusion

Based on the VASP simulation package we have conducted a series of calculations of transition metal dopants in Bi_2WO_6. We have calculated the structural relaxation, DOS, and optical absorption coefficient of Bi_2WO_6 doped with Mo, Cr, Fe, and Zn. All the dopants contribute to the reduction of the band gap and help improve the ability of optical absorption in the visible range. This behavior has been explained by the presence of deep impurity states within the band gap. However, for Zn–doped Bi_2WO_6, the band reduction is a consequence of shifting the top of the valence band under the influence of the Zn $3d$–levels. Among the investigated dopants, Zn could be considered the best candidate for improving the optical characteristics of Bi_2WO_6 owing to the calculated band narrowing without a direct presence of localized defect states in the band gap. In addition, Zn doping on W lattice site does not seem to affect the mobility of the generated charges, as reflected in the relatively unperturbed widths of the VB and CB of this material.

7. Acknowledgements

The authors would like to acknowledge the generous donation by the NVIDIA Corporation via their GPU Grant Program, which helped accelerate the computations done in this work. The financial support for this study was provided by the Ministry of Education, Science and Technological Development of the Republic of Serbia, through the project no. 171001.

References

[1] J. M. Coronado, F. Fresno, M. D. Hernández-Alonso, R. Portela, Design of Advanced Photocatalytic Materials for Energy and Environmental Applications, Green Energy and Technology, Springer-Verlag, London, 2013. `doi:10.1007/978-1-4471-5061-9`.

[2] S. Girish Kumar, K. Koteswara Rao, Tungsten-based nanomaterials (WO_3 & Bi_2WO_6): Modifications related to charge carrier transfer mechanisms and photocatalytic applications, Applied Surface Science 355 (2015) 939–958. `doi:10.1016/j.apsusc.2015.07.003`.

[3] H. Fu, L. Zhang, W. Yao, Y. Zhu, Photocatalytic properties of nanosized Bi_2WO_6 catalysts synthesized via a hydrothermal process, Applied Catalysis B: Environmental 66 (2006) 100–110. `doi:10.1016/j.apcatb.2006.02.022`.

[4] L. Yan, Y. Wang, H. Shen, Y. Zhang, J. Li, D. Wang, Photocatalytic activity of Bi_2WO_6/Bi_2S_3 heterojunctions: the facilitation of exposed facets of Bi_2WO_6 substrate, Applied Surface Science 393 (2017) 496–503. `doi:10.1016/j.apsusc.2016.10.039`.

[5] H. Fu, C. Pan, L. Zhang, Y. Zhu, Synthesis, characterization and photocatalytic properties of nanosized Bi_2WO_6, $PbWO_4$ and $ZnWO_4$ catalysts, Materials Research Bulletin 42 (2007) 696–706. `doi:10.1016/j.materresbull.2006.07.017`.

[6] J. Ren, W. Wenzhong, L. Zhang, J. Chang, S. Hu, Photocatalytic inactivation of bacteria by photocatalyst Bi_2WO_6 under visible light, Catalysis Communications 10 (14) (2009) 1940–1943. `doi:10.1016/j.catcom.2009.07.006`.

[7] L. Zhang, H. Wang, Z. Chen, P. K. Wong, J. Liu, Bi_2WO_6 micro/nanostructures: Synthesis, modifications and visible-light-driven photocatalytic applications, Applied Catalysis B: Environmental 106 (1) (2011) 1–13. `doi:10.1016/j.apcatb.2011.05.008`.

[8] T. Saison, P. Gras, N. Chemin, C. Chanéac, O. Durupthy, V. Brezová, C. Colbeau-Justin, J.-P. Jolivet, New insights into Bi_2WO_6 properties as a visible-light photocatalyst, The Journal of Physical Chemistry C 117 (44) (2013) 22656–22666. `doi:10.1021/jp4048192`.

[9] N. Tian, Y. Zhang, H. Huang, Y. He, Y. Guo, Influences of Gd Substitution on the Crystal Structure and Visble-Light-Driven Photocatalytic Performance of Bi_2WO_6, The Journal of Physical Chemistry C 118 (2014) 15640–15648. `doi:10.1021/jp500645p`.

[10] S. Guo, X. Li, H. Wang, F. Dong, Z. Wu, Fe-ions modified mesoporous Bi_2WO_6 nanosheets with high visible light photocatalytic activity, Journal of Colloid and Interface Science 369 (1) (2012) 373–380. `doi:10.1016/j.jcis.2011.12.007`.

[11] L. Zhang, Y. Man, Y. Zhu, Effects of Mo Replacement on the Structure and Visible-Light-Induced Photocatalytic Performances of Bi_2WO_6 photocatalyst, ACS Catalysis 1 (8) (2011) 841–848. `doi:10.1021/cs200155z`.

[12] R. Shi, G. Huang, J. Lin, Y. Zhu, Photocatalytic Activity Enhancement for Bi_2WO_6 by Fluorine Substitution, Journal of Physical Chemistry C 113 (45) (2009) 19633–19638. `doi:10.1021/jp906680e`.

[13] Y. Wei, X. Wei, S. Guo, Y. Huang, G. Zhu, J. Zhang, The effects of Br

dopant on the photo-catalytic properties of Bi_2WO_6, Materials Science and Engineering B 206 (2016) 79–84. `doi:10.1016/j.mseb.2015.12.004`.

[14] P. Dumrongrojthanath, A. Phuruangrat, S. Thongstem, T. Thongstem, Hydrothermal preparation of visble-light-driven Br-doped Bi_2WO_6 photocatalyst, Materials Letters 209 (2017) 501–504. `doi:10.1016/j.matlet.2017.08.089`.

[15] A. H. Ahsaine, A. Eljaouhari, A. Slassi, M. Ezahri, A. Benlhachemi, B. Bakiz, F. Guinneton, J. R. Gavarri, Electronic band structure and visible-light photocatalytic activity of Bi_2WO_6: elucidating the effect of lutetium doping, RSC Advances 6 (2016) 101105–101114. `doi:10.1039/C6RA22669H`.

[16] R. Chen, C. H. Hu, S. Wei, J. H. Xia, J. Cui, H. Y. Zhou, Synthesis and Activity of Ag-Doped Bi_2WO_6 Photocatalysts, in: Energy and Environment Materials, Vol. 743 of Materials Science Forum, Trans Tech Publications Ltd, 2013, pp. 560–566. `doi:10.4028/www.scientific.net/MSF.743-744.560`.

[17] J. Wang, X. Gao, F. Fu, L. Zhang, Y. Wu, Photocatalytic Degradation of Phenol-containing Wastewater over Cu-Bi_2WO_6 Composite under Visible Light Irradiation, Journal of Residuals Science and Technology 9 (3) (2012) 101–106.
URL `https://www.destechpub.com/wp-content/uploads/2019/01/JRST-Volume-9-Number-3-July-2012.pdf?x82929`

[18] X. C. Song, Y. F. Zheng, M. Rong, Y. Y. Zhang, H. Y. Yin, Photocatalytic activities of Mo-doped Bi_2WO_6 three-dimensional hierarchical microspheres, Journal of Hazardous Materials 192 (1) (2011) 186–191. `doi:10.1016/j.jhazmat.2011.05.001`.

[19] C. Bhattacharya, H. C. Lee, A. J. Bard, Rapid Screening by Scanning Electrochemical Microscopy (SECM) of Dopants for Bi_2WO_6 Improved

Photocatalytic Water Oxidation with Zn Doping, The Journal of Physical Chemistry C 117 (19) (2013) 9633–9640. `doi:10.1021/jp308629q`.

[20] Z. Zhang, W. Wang, E. Gao, M. Shang, J. Xu, Enhanced photocatalytic activity of Bi_2WO_6 with oxygen vacancies by zirconium doping, Journal of Hazardous Materials 196 (2011) 255–262. `doi:10.1016/j.jhazmat.2011.09.017`.

[21] W. Zhang, N. Yu, L. Zhang, K. Jiang, Y. Chen, Z. Chen, Synthesis of Yb^{3+}/Er^{3+} co-doped Bi_2WO_6 nanosheets with enhanced photocatalytic activity, Materials Letters 163 (2016) 16–19. `doi:10.1016/j.matlet.2015.09.113`.

[22] Y. Su, G. Tan, C. Xu, T. Liu, Y. Wang, H. Ren, A. Xia, The up-conversion effect induced NIR-photocatalytic performance of $Bi_{2-x}Er_xWO_6$ photocatalysts, Materials Letters 211 (2018) 175–178. `doi:10.1016/j.matlet.2017.09.115`.

[23] M. Wang, Z. Qiao, M. Fang, Z. Huang, Y. Liu, X. Wu, C. Tang, H. Tang, H. Zhu, Synthesis of Er-doped Bi_2WO_6 and enhancement in photocatalytic activity induced by visible light, RSC Advances 5 (2015) 94887–94894. `doi:10.1039/C5RA19164E`.

[24] R. M. Mohamed, E. S. Aazam, Enhancement of photocatalytic properties of Bi_2WO_6 nanoparticles by Pt deposition, Materials Research Bulletin 48 (9) (2013) 3572–3578. `doi:10.1016/j.materresbull.2013.05.062`.

[25] Y. Liu, W. Wang, Z. Fu, H. Wang, Y. Wang, J. Zhang, Nest-like strucures of Sr doped Bi_2WO_6: synthesis and enhanced photocatalytic properties, Materials Science and Engineering B 176 (16) (2011) 1264–1270. `doi:10.1016/j.mseb.2011.07.014`.

[26] X. C. Song, W. T. Li, W. Z. Huang, H. Zhou, H. Y. Yin, Y. F. Zheng, Enhanced photocatalytic activity of cadmium-doped Bi_2WO_6 nanoparticles

under simulated solar light, Journal of Nanoparticle Research 17 (3) (2015) 134. `doi:10.1007/s11051-015-2945-1`.

[27] X. Xu, Y. Ge, B. Li, F. Fan, F. Wang, Shape evolution of Eu-doped Bi_2WO_6 and their photocatalytic properties, Materials Research Bulletin 59 (2014) 329–336. `doi:10.1016/j.materresbull.2014.07.050`.

[28] W. T. Li, W. Z. Huang, H. Zhou, H. Y. Yin, Y. F. Zheng, X. C. Song, Synthesis and photoactivity enhancement of Ba doped Bi_2WO_6 photocatalyst, Materials Research Bulletin 64 (2015) 432–437. `doi:10.1016/j.materresbull.2015.01.023`.

[29] K. Lai, Y. Zhu, J. Lu, Y. Dai, B. Huang, N- and Mo-doping Bi_2WO_6 in photocatalytic water splitting, Computational Materials Science 67 (2013) 88–92. `doi:10.1016/j.commatsci.2012.08.024`.

[30] Y. Zhang, Y. Ma, Q. Liu, H. Jiang, Q. Wang, D. Qu, J. Shi, Synthesis of Er^{3+}/Zn^{2+} co-doped Bi_2WO_6 with highly efficient photocatalytic performance under natural indoor weak light illumination, Ceramics International 43 (2) (2017) 2598–2605. `doi:10.1016/j.ceramint.2016.11.069`.

[31] F. Ren, J. Zhang, Y. Wang, Enhanced photocatalytic activities of Bi_2WO_6 by introducing Zn to replace Bi lattice sites: a first-principles study, RSC Adv. 5 (2015) 29058–29065. `doi:10.1039/C5RA02735G`.

[32] G. Kresse, J. Furthmüller, Efficient iterative schemes for *ab initio* total-energy calculations using a plane-wave basis set, Phys. Rev. B 54 (1996) 11169–11186. `doi:10.1103/PhysRevB.54.11169`.

[33] G. Kresse, D. Joubert, From ultrasoft pseudopotentials to the projector augmented-wave method, Phys. Rev. B 59 (1999) 1758–1775. `doi:10.1103/PhysRevB.59.1758`.

[34] J. P. Perdew, K. Burke, M. Ernzerhof, Generalized Gradient Approximation Made Simple, Phys. Rev. Lett. 77 (1996) 3865–3868. `doi:10.1103/PhysRevLett.77.3865`.

[35] H. J. Monkhorst, J. D. Pack, Special points for Brillouin-zone integrations, Phys. Rev. B 13 (1976) 5188–5192. `doi:10.1103/PhysRevB.13.5188`.

[36] D. A. Rae, J. G. Thompson, R. L. Withers, Structure Refinement of Commensurately Modulated Bismuth Tungstate, Bi_2WO_6, Acta Crystallographica Section B 47 (6) (1991) 870–881. `doi:10.1107/S0108768191008030`.

[37] N. A. McDowell, K. S. Knight, P. Lightfoot, Unusual High-Temperature Structural Behaviour in Ferroelectric Bi_2WO_6, Chemistry A European Journal 12 (5) (2006) 1493–1499. `doi:10.1002/chem.200500904`.

[38] H. Djani, P. Hermet, P. Ghosez, First-Principles Characterization of the $P21ab$ Ferroelectric Phase of Aurivillius Bi_2WO_6, The Journal of Physical Chemistry C 118 (25) (2014) 13514–13524. `doi:10.1021/jp504674k`.

[39] S. R. Bahn, K. W. Jacobsen, An object-oriented scripting interface to a legacy electronic structure code, Computing in Science & Engineering 4 (3) (2002) 56–66. `arXiv:https://aip.scitation.org/doi/pdf/10.1109/5992.998641`, `doi:10.1109/5992.998641`.
URL `https://aip.scitation.org/doi/abs/10.1109/5992.998641`

[40] F. Tran, P. Blaha, Importance of the kinetic energy density for band gap calculations in solids with density functional theory, The Journal of Physical Chemistry A 121 (17) (2017) 3318–3325, pMID: 28402113. `doi:10.1021/acs.jpca.7b02882`.

[41] A. Kudo, S. Hijii, H_2 or O_2 Evolution from Aqueous Solutions on Layered Oxide Photocatalysts Consisting of Bi^{3+} with $6s^2$ Configuration and d^0 Transition Metal Ions, Chemistry Letters 28 (10) (1999) 1103–1104. `doi:10.1246/cl.1999.1103`.

[42] Y. Zhou, Y. Zhang, M. Lin, J. Long, Z. Zhang, H. Lin, J. C. S. Wu, X. Wang, Monolayered Bi_2WO_6 nanosheets mimicking heterojunction in-

terface with open surfaces for photocatalysis, Nature Communications 6 (2015) 8340. `doi:10.1038/ncomms9340`.

[43] M. Teck, M. M. Murshed, M. Schowalter, N. Lefeld, H. K. Grossmann, T. Grieb, T. Hartmann, L. Robben, A. Rosenauer, L. Mädler, T. M. Gesing, Structural and spectroscopic comparison between polycrystalline, nanocrystalline and quantum dot visible light photo-catalyst Bi_2WO_6, Journal of Solid State Chemistry 254 (2017) 82–89. `doi:10.1016/j.jssc.2017.07.013`.

[44] J. Tang, Z. Zou, J. Ye, Photocatalytic decomposition of organic contaminants by Bi_2WO_6 under visible light irradiation, Catalysis Letters 92 (1–2) (2004) 53–56. `doi:10.1023/B:CATL.0000011086.20412.aa`.

[45] A. V. Krukau, O. A. Vydrov, A. F. Izmaylov, G. E. Scuseria, Influence of the exchange screening parameter on the performance of screened hybrid functionals, The Journal of Chemical Physics 125 (22) (2006) 224106. `doi:10.1063/1.2404663`.

[46] J. Paier, M. Marsman, K. Hummer, G. Kresse, I. C. Gerber, J. G. Ángyán, Screened hybrid density functionals applied to solids, The Journal of Chemical Physics 124 (15) (2006) 154709. `doi:10.1063/1.2187006`.

[47] L. Zhou, M. Yu, J. Yang, Y. Wang, C. Yu, Nanosheet-Based $Bi_2Mo_xW_{1-x}O_6$ Solid Solutions with Adjustable Band Gaps and Enhanced Visible-Light-Driven Photocatalytic Activities, The Journal of Physical Chemistry C 114 (44) (2010) 18812–18818. `doi:10.1021/jp107061p`.